

## Condensation of eigenmodes in functional brain network and its correlation to chimera state

Siyu Huo <sup>1</sup> & Zonghua Liu <sup>1</sup>✉

Condensation has long been a closely studied problem in statistical physics but little attention has been paid to neural science. Here, we discuss this problem in brain networks and discover the condensation of a functional brain network whereby all its eigenmodes are condensed only into a few or even a single eigenmode of the structural brain network. We show that the condensation occurs due to the emergence of both chimera states and brain functions from the structure of the brain network. Furthermore, the condensation only appears in the regions of chimera and the condensed eigenmodes are only limited to the lower ones. Condensation is confirmed across different levels of brain subnetworks, including hemispheres, cognitive subnetworks, and isolated cognitive subnetworks, which are further supported by resting-state functional connectivity from empirical data. Our results indicate that condensation could be a potential mechanism for performing brain functions.

<sup>1</sup>State Key Laboratory of Precision Spectroscopy and School of Physics and Electronic Science, East China Normal University, Shanghai, PR China.  
✉email: [zhliu@phy.ecnu.edu.cn](mailto:zhliu@phy.ecnu.edu.cn)

In statistical physics, condensation has long been an interesting topic that has attracted a much attention. For example, it was first shown in 1920 that Bose gas is condensed in the momentum space when the temperature is lower than the critical point, called the *Bose-Einstein condensation* (BEC). Then, it was shown in 2001 that BEC may also occur in complex networks where the phenomenon of “winner-takes-all” is observed in competitive systems<sup>1</sup>. Recently work showed that there is a condensation of the eigen microstate in nonequilibrium complex systems such as the climate systems and ecosystems<sup>2</sup>. Thus, condensation is generally related to phase transitions and critical phenomena. On the other hand, it is well known that our brain system works at a critical point that enables its significant flexibility to accomplish various functions<sup>3</sup>. Thus, a natural question arises: Does the performance of each specific brain function have any relevance to condensation?

Understanding this is a nontrivial task since it is closely related to the key question in brain sciences, i.e., how brain functions emerge from brain structural networks. In fact, the understanding of the human brain has long been a scientific endeavor<sup>4,5</sup>. It is now well known that human brain networks show a variety of spatiotemporal patterns, which are often characterized by two closely related aspects, i.e., structural and functional brain networks<sup>6–8</sup>. The former can be further divided into different subnetworks according to specific features over multiple spatial scales, such as hemispheres and cognitive networks<sup>9,10</sup>. On the other hand, the latter reflects dynamic interactions between functionally specialized but widely distributed cortical regions, which are often obtained by Pearson correlations between measured EEG time series<sup>11</sup>. One interesting question concerns how the structural network supports the functional network and the resulting flexible and adaptive human behaviors. Significant achievements have been made in the fields of nonlinear dynamics and complex networks. It was found that the unique topology of brain networks plays key roles in the emergence of collective behaviors, such as chimera state, remote synchronization, clustering synchronization, and remote propagation<sup>12–14</sup>. More specifically, the chimera state represents the coexistence of one completely synchronized part and another completely desynchronized part that has been intensely studied in neuronal networks. Prior work showed that there are many chimera-like behaviors in neuronal functions, including unihemispheric sleep, neural bumps, and even some pathological diseases such as Parkinson’s disease, Alzheimer’s disease, etc.<sup>15–18</sup>. Notably, the chimera state was confirmed in the human brain network in 2016 that the default-mode network in one hemisphere is kept more vigilant to wake the sleeper up as a night watch upon detection of deviant stimuli, called the *first-night effect* in human sleep, when humans sleep in a novel environment<sup>19</sup>.

Similarly, Bansal et al. further presented a chimera-based framework to explore how large-scale brain architecture affects brain dynamics and function<sup>9</sup>. They found that the emergent dynamical patterns across predefined cognitive systems are closely related to structural variability, which are termed *cognitive chimera states*. However, it remains unclear how these chimera states are produced by the brain structural network. Therefore, we study this problem from the perspective of eigenmode analysis and find an interesting phenomenon of condensation, i.e., all eigenmodes of a functional brain network are condensed to a few or even a single eigenmode of the structural brain network in the region of chimera states. This finding reveals a potential mechanism for describing brain functions.

Spectral graph theory has been used to study the relationship between structural and functional networks<sup>20</sup>, where it was not apparent at the node-pair level but rather at the level of the eigen-spectra of the brain graph. By this method, it was shown that the

eigenvectors of the connectome Laplacian are good predictors of functional eigenvectors<sup>20–23</sup>. Recently, eigenmode analysis was extended to investigate the joint contribution of hierarchical modular structural organization and critical state to brain functional diversity<sup>24,25</sup>.

In this work, we use eigenmode analysis to study the underlying mechanism of cognitive chimera states. We find that in the region of chimera states, all the eigenmodes of a functional brain network may be condensed to a few or even a single eigenmode of structural brain network and the condensed eigenmodes are limited to lower modes. Furthermore, we show that the contributions of structural eigenmodes satisfy distinct distributions in the regions of chimera and nonchimera states, i.e., a power law distribution describes the former while an exponential distribution describes the latter. These results are confirmed across different levels of brain subnetworks, such as hemispheres, cognitive subnetworks, isolated cognitive subnetworks, as well as by the empirical data of resting-state functional connectivity (rsFC), thus indicating a close relationship between the condensation of eigenmodes and the chimera state.

### A neural mass model of a brain network

To study the dynamics of the brain network, we adopt the networked dynamics model of Ref. <sup>8</sup>. For the network substrate, we employ the weighted network of the cerebral cortex from the data of Refs. <sup>26,27</sup>, which is further divided into  $N = 989$  connected cortical regions (ROIs). Each ROI is regarded as a network node, and the connections between all possible pairs of ROIs were measured noninvasively by diffusion spectrum imaging (DSI). Additional details are provided in the Methods section. With this approach, a connection between two ROIs was derived from the number of fibers found by the tractography algorithm, which results in 17,865 connections. The obtained network consists of  $N_r = 496$  nodes in the right hemisphere and  $N_l = 493$  nodes in the left hemisphere, and its  $N \times N$  connection matrix  $\{W_{IJ}\}$  is weighted<sup>8</sup>. Fig. 1a, b show the distribution of nodes and the connection matrix  $\{W_{IJ}\}$ , respectively.

For the node dynamics, we adopt the neural mass model describing the mean field activity of a neuronal population<sup>28,29</sup>. This low-dimensional model with biologically plausible interactions between excitatory and inhibitory neural populations can generate oscillations in the alpha band ( $\sim 10$  Hz) and is used to represent resting brain states<sup>30</sup>. Increasing evidence shows that the local circuits in the cortical regions are not identical<sup>31</sup> but display heterogeneity in neuronal density and spine density *etc.* However, modeling the regions with a simplified assumption of identical neural mass oscillators allows us to focus on the effect of the underlying network architecture on the dynamical patterns. The dynamical equations of identical neural mass oscillators are coupled to the underlying cortical network as

$$\begin{aligned} \dot{v}_I^p &= Aaf(v_I^e - v_I^i) - 2av_I^p - a^2v_I^p, \\ \dot{v}_I^i &= BbC_4f(C_3v_I^p) - 2bv_I^i - b^2v_I^i, \\ \dot{v}_I^e &= Aa[C_2f(C_1v_I^p) + p_I + \frac{c}{w_I} \sum_{J=1}^N W_{IJ}(v_J^e(t - \tau) - v_I^e)] \\ &\quad - 2av_I^e - a^2v_I^e, \end{aligned} \quad (1)$$

where  $I = 1, \dots, N$ ,  $v_I^p$ ,  $v_I^i$  and  $v_I^e$  are the postsynaptic membrane potentials for three subpopulations (pyramidal neurons, inhibitory and excitatory interneurons) of node- $I$ . The sigmoid function  $f(v)$  converts the average membrane potential into an average pulse density of action potentials (spikes), which propagate among subpopulations within each node and between nodes through synaptic coupling. The parameters  $A$  and  $B$  represent the average synaptic gains,  $1/a$  and  $1/b$  are the average

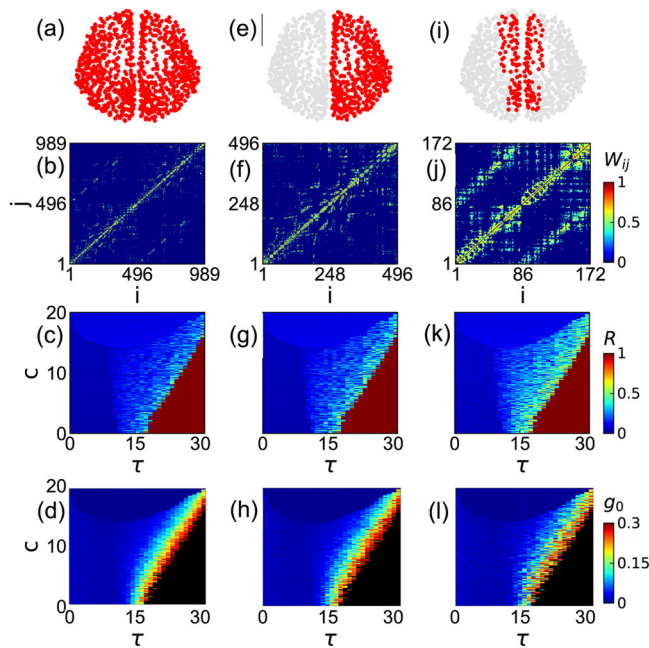


**Fig. 1** Different levels of brain networks and their connectivity matrices.

The dynamics are calculated for a global brain network. **a–d** global brain network, **e–h** right hemisphere, and **i–l** the cognitive network of the medial default mode. The first row of **a**, **e**, and **i** represents the node distributions of the three cases on the cerebral cortex, where the red dots represent the nodes and their locations. The second row of **b**, **f**, and **j** represents the connection matrix  $\{W_{ij}\}$  of the three cases. The network size is  $N = 989$  in **b**,  $N_r = 496$  in **f**, and  $N_m = 172$  in **j**. The third row of **c**, **g** and **k** represents the phase diagrams of  $R$  on the parameter space  $\tau - c$  plane for the three cases, respectively, with  $\tau$  being the time delay and  $c$  being the coupling strength. The four rows of **d**, **h**, and **l** represent the phase diagrams of  $g_0$  on the parameter space  $\tau - c$  plane for the three cases, respectively.

dendritic-membrane time constants.  $C_1$  and  $C_2$ ,  $C_3$  and  $C_4$  are the average number of synaptic contacts among the subpopulations. A more detailed interpretation and the standard parameter values of this model can be found in<sup>28,29</sup>. In this work, we follow Ref. 29 to take the parameters as  $cc = 135$ ,  $C1 = cc$ ,  $C2 = 0.8cc$ ,  $C3 = 0.25cc$ ,  $C4 = 0.25cc$ ,  $A = 3.25$ ,  $B = 22$ ,  $a = 100$ ,  $b = 50$ , and  $p_I = 180$ . The sigmoid function takes the form  $f(v) = 2e_0 / (1 + e^{r(v_0 - v)})$ , where  $v_0$  is the post-synaptic potential corresponding to a firing rate of  $e_0$ , and  $r$  is the steepness of the activation, with the parameters as  $v_0 = 6$ ,  $e_0 = 2.5$ , and  $r = 0.56$  as in Refs. 28,29.  $W_{IJ}$  is the coupling matrix with the real connection weights from the data of Refs. 26,27. The coupling strength  $c$  is normalized by the mean intensity  $w_I$  across the nodes, where  $w_I = \sum_j^N W_{IJ}$  is the total input weight to node- $I$ .  $\tau$  is the time delay for interregional signal transmission, which is assumed to be common for different links. In physical brains, the finite signal transmission speed leads to measurable time delays, especially through those links traversing the corpus callosum and gyrus, where such delays can be up to several tens of milliseconds<sup>32–39</sup>.

To study the dynamics of Eq. (1), we perform extensive numerical simulations by choosing different  $\tau$  and  $c$ . As in Refs. 28,29, we take the average potential  $u_I = v_I^r - v_I^i$  to represent the local field potential. We find that various dynamic patterns emerge from the underlying brain structural network under different pairs of parameter settings  $(\tau, c)$ ; see Fig. S2 in Supplementary Note 1 for typical patterns. An efficient index to describe these dynamics is the order parameter  $R$  defined by Eq. (2). Fig. 1c shows the phase diagram of  $R$  on the parameter space  $\tau - c$  plane for the global brain network, with  $N_s = N$  in

Eq. (2). We observe that the states of  $0 < R < 1$  only appear in a narrow region with  $c$  is proportional to  $\tau$ . Beyond this narrow range, the state will be either disorder ( $R \approx 0$ ) in the upper-left part or synchronized ( $R \approx 1$ ) in the lower-right part. In the narrow range of  $0 < R < 1$ , we find that the spatiotemporal patterns are similar to the chimera patterns of Fig. S2 in Supplementary Note 1, i.e., coexistence of synchronization and dyssynchronization, indicating this to be a region of chimera states.

To conveniently characterize the chimera state, Kemeth et al. introduced an index  $g_0$  defined by Eq. (4) describes the fraction of synchronization<sup>40</sup>. Fig. 1d shows the phase diagram of  $g_0$ . Comparing it with Fig. 1c, we observe similar patterns, confirming that the chimera states exist only in the narrow region, with  $c$  being proportional to  $\tau$ .

It is therefore natural to ask whether it is possible to observe results similar to those of Fig. 1c, d at the hemispherical level. This question is not trivial, as the damage to specialized brain regions results in behavioral impairments, even though most major brain functions remain intact, as exemplified by famous clinical case studies such as Phineas Gage<sup>4</sup> and H.M.<sup>5</sup>. To study this problem, we run the dynamics of the global brain network but calculate the quantities  $R$  and  $g_0$  only for the subnetwork of the right hemisphere. Fig. 1g and h show the results where  $R$  and  $g_0$  are calculated only for the nodes on the right hemisphere, i.e.,  $N_s = N_r$  in Eqs. (2) and (4). We observe that their phase diagrams are similar to Fig. 1c, d, respectively, confirming the brain functions in the right hemisphere. Correspondingly, Fig. 1e, f show its nodes' distribution and connection matrix  $\{W_{ij}\}$ , respectively.

However, individual brain functions are in fact performed by cognitive networks rather than the global network or broader hemispheres; thus, it is more appropriate to study the phase diagrams of  $R$  and  $g_0$  at the level of cognitive networks. Toward this goal, we follow Ref. 9 to classify the brain network into eight cognitive networks; see Figs. S4 and S5 in Supplementary Note 1 for details. Then, we calculate the phase diagrams of  $R$  and  $g_0$  for each cognitive network. Interestingly, we observe similar results as in Fig. 1c, d for each cognitive network. As an example, Fig. 1k, l show the results for the cognitive network of medial default mode with the number of total nodes  $N_m = 172$ . Correspondingly, Fig. 1i, j show its nodes' distribution and connection matrix  $\{W_{ij}\}$ , respectively. In summary, from the third and fourth rows of Fig. 1 shows that chimera states can be observed in all three levels of the brain network and their chimera regions in the parameter space  $\tau - c$  plane are consistent with each other, indicating that some hidden feature exists.

## Results

**Case of a globally connected brain network.** We now discuss the condensation of eigenmodes of a functional brain network. Numerically, we first calculate all the time series  $u_I(t)$  from Eq. (1) for  $I = 1, 2, \dots, N$  and then follow Eq. (7) to obtain  $S_c(j)$  step by step. However, we find that the contribution  $S_c(1)$  from the trivial eigenmode with  $\lambda_1 = 0$  is always relatively large for different  $(\tau, c)$  and thus prevent us from obtaining useful information from other structural eigenmodes. To overcome this problem, we follow Ref. 24 to artificially set  $S_c(1) = 0.1$ , noting that this procedure does not have a significant impact on the results. In this way, Fig. 2a and b show the distribution of  $S_c(j)$  for two typical cases, where the parameters are taken as  $(c = 5.3, \tau = 19)$  in (a) and  $(c = 0.3, \tau = 9)$  in (b). We observe from Fig. 2a that there is a dominant  $S_c(12)$  (i.e., the dot in the red circle for visualization), which is much larger than others, indicating that the functional network is mainly a result of the contribution of the twelfth structural eigenmode. We denote this as condensation on the

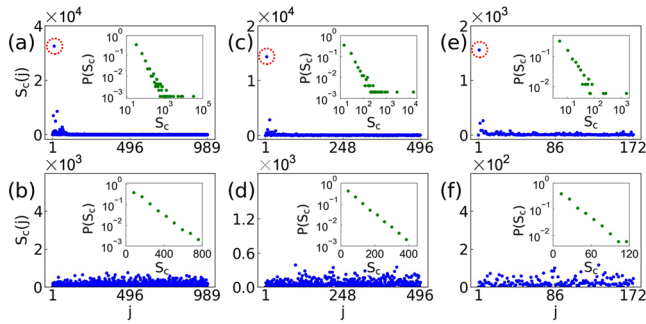


**Fig. 2 The contributions  $S_c(j)$  of the  $j$ -th structural eigenmode for the cases of typical condensation and noncondensation.** The insets represent their distributions  $P(S_c)$ . The first row represents the case of typical condensation where there is a significant  $S_c(j)$  in each panel, i.e., the dot in the red circle, which is much larger than the others. The second row represents the case of noncondensation where there is no significant  $S_c(j)$  in each panel. **a, b** represent the case of a global brain network corresponding to Fig. 1a, where the parameters are taken as  $(c = 5.3, \tau = 19)$  in **a** and  $(c = 0.3, \tau = 9)$  in **b**. **c, d** represent the network of the right hemisphere corresponding to Fig. 1e, where the parameters are taken as  $(c = 5.3, \tau = 21)$  in **c** and  $(c = 1.9, \tau = 9)$  in **d**. **e, f** represent the cognitive network of medial default mode corresponding to Fig. 1i, where the parameters are taken as  $(c = 7.3, \tau = 22)$  in **e** and  $(c = 11.5, \tau = 10)$  in **f**.

twelfth structural eigenmode. In contrast, we observe from Fig. 2b that there is no dominant  $S_c(j)$ , indicating no condensation.

To better understand this condensation phenomenon, we calculate the distribution of  $S_c(j)$  for each set of  $S_c(j)$  ( $j = 1, 2, \dots, N$ ). The insets of Fig. 2a, b show their distributions,  $P(S_c)$ , respectively. In the inset of Fig. 2a, we interestingly find that  $P(S_c)$  depends linearly on  $S_c$  in the log-log plot, indicating that the distribution  $P(S_c)$  is a power law. In the inset of Fig. 2b, we further find that  $P(S_c)$  depends linearly on  $S_c$  in the log-linear plot but not in the log-log plot, indicating that the distribution  $P(S_c)$  is exponential. Therefore, the distributions  $P(S_c)$  in the regions of the chimera state and nonchimera state are fundamentally different. The human brain is evidenced to be near the critical state when the power law distribution is one of its characteristic features<sup>3</sup>. Therefore, the power law of  $P(S_c)$  in Fig. 2a may imply that condensation is in fact a possible mechanism for describing brain function.

We therefore ask: Do the observations in Fig. 2a, b also exist at the levels of hemispheres and cognitive networks? To address this question, Fig. 2c, d show the results of the right hemisphere, with  $(c = 5.3, \tau = 21)$  in (c) and  $(c = 1.9, \tau = 9)$  in (d). The data clearly show that there are dominant  $S_c(5)$  in Fig. 2c (see the dot in the red circle) but no dominant one in (d), confirming the condensation in (c). The insets of Fig. 2c, d also show that the distribution  $P(S_c)$  is a power law in (c) but exponential in (d), confirming again that condensation is closely related to the power law distribution. Similarly, we find the condensation and power law distribution for the cognitive network of the medial default mode, as shown in Fig. 2e and (f), where the dominant mode in (e) is  $S_c(2)$  (see the dotted red circle). This type of condensation on a single structural eigenmode is more of an outlier; more general cases describe the condensation on a few structural eigenmodes, as shown by Fig. S9 in Supplementary Note 2.A.

Figure 2a-f only depict a few typical sets of parameters  $(\tau, c)$ . To perform a full study on the phase plane of  $(\tau, c)$ , we notice from Fig. 2a, b that  $S_c(j)$  has a much larger fluctuation in (a) than in (b), indicating that we can use the standard deviation  $\sigma(\tau, c) = \sqrt{\frac{1}{N} \sum_{j=1}^N (S_c(j) - \langle S_c(j) \rangle)^2}$  as an index to help us understand

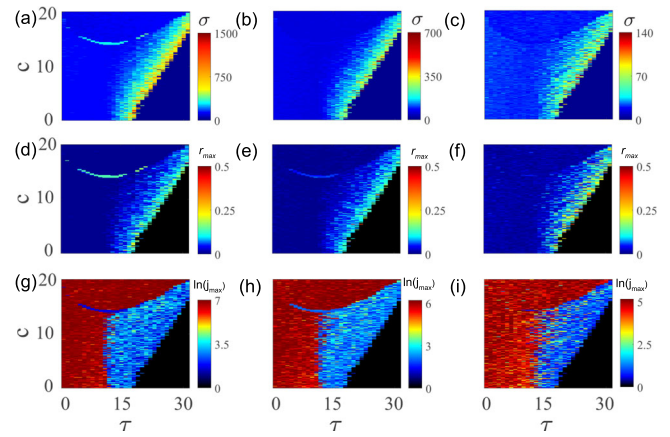


**Fig. 3 Three extra indices characterize the condensation.**  $\sigma, j_{max}$  and  $r_{max}$  represent the standard deviation, the maximum structural eigenmode, and the ratio of the contribution of the maximum structural eigenmode to the total contribution of all the structural eigenmodes, respectively. The first to third columns represent the cases of the global brain network, the right hemisphere, and the cognitive network of medial default mode, respectively. **a-c** represent the phase diagrams of  $\sigma(\tau, c)$  on the parameter space  $\tau - c$  plane, where **a-c** correspond to the cases of Fig. 1a-c, respectively. **d-f** represent the phase diagrams of  $r_{max}$  corresponding to **a-c**, respectively. and **g-i** distributions of  $j_{max}$  corresponding to **a-c**, respectively.

condensation. Based on this index, Fig. 3a-c show the phase diagrams of  $\sigma(\tau, c)$  on the parameter space  $\tau - c$  plane, where (a)-(c) correspond to the cases of Fig. 1d, h, and l. Interestingly, we find that Fig. 3a-c are similar to Fig. 1d, h, and l, respectively, indicating that the regions of larger deviation in Fig. 3a-c are closely related to the narrow regions of chimera states in Fig. 1d, h, and l.

Considering that a larger deviation may also be induced by a large fluctuation rather than condensation, we need to introduce some extra indices. For this purpose, first determine the maximum of  $S_c(j)$  for each pair of  $(\tau, c)$  and let it be  $S_c(j_{max})$ . Then, we let  $r_{max} = S_c(j_{max}) / \sum_{j=1}^N S_c(j)$  be the index, i.e., the ratio of  $S_c(j_{max})$  to the sum of  $S_c(j)$ . A larger  $r_{max}$  will represent a stronger degree of condensation. Fig. 3d-f shows the phase diagrams of  $r_{max}$  corresponding to (a-c), respectively. Comparing Fig. 3d-f with a-c, we see that they are consistent with each other, indicating that a larger  $\sigma(\tau, c)$  corresponds to a larger  $r_{max}$ .

It is also interesting to study the condensed eigenmode, i.e.,  $j_{max}$ . For this purpose, Fig. 3g-i show the distributions of  $j_{max}$  corresponding to a-c, respectively. Each phase diagram is clearly divided into three distinct “red”, “blue” and “black” regions, which respectively indicate a clear boundary between the condensed region and the disordered region or between the condensed region and the synchronized region. Notably, all the blue regions have smaller values of  $j_{max}$ , implying that condensation is limited only to the lower structural eigenmodes.

Based on these three indices of  $\sigma, j_{max}$  and  $r_{max}$  we find a one-to-one correspondence between the condensation of Fig. 3 and the chimera states of Fig. 1. For the synchronization, we have  $R = 1$  and  $g_0 = 1$  in Fig. 1 and  $\sigma = 0$  in Fig. 3. For the disordered state, we have  $R \approx 0$  and  $g_0 \approx 0$  in Fig. 1 and  $r_{max} \approx 0$  in Figure 3. For the chimera states, we have  $0 < R < 1$  and  $0 < g_0 < 1$  in Fig. 1 and the maximum  $\sigma$  and  $r_{max}$  but lower  $j_{max}$  in Fig. 3. These correspondences indicate that there is a close relationship between the chimera state and condensation.

Moreover, it is useful to show a few condensed structural eigenmodes for visualization. For this purpose, Fig. 4 shows six

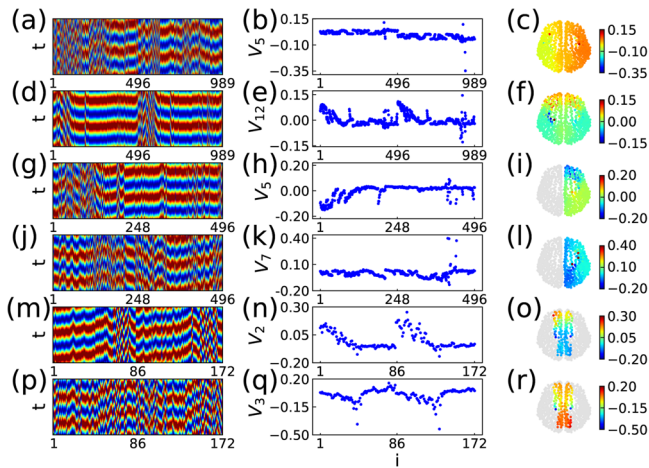


**Fig. 4 Six typical condensations with the lower condensed eigenmodes.** **a-c** and **d-f** represent the case of global brain network with ( $c = 0.325, \tau = 16$ ) in **a-c** and ( $c = 0.025, \tau = 16$ ) in **d-f**, **g-i** and **j-l** the case of right hemisphere with ( $c = 0.15, \tau = 16$ ) in **g-i** and ( $c = 0.85, \tau = 15$ ) in **j-l**, and **m-o**, and **p-r** the case of the cognitive network of medial default mode with ( $c = 0.775, \tau = 17$ ) in **m-o** and ( $c = 0.75, \tau = 15$ ) in **p-r**. The left column of **a, d, g, j, m**, and **p** represents the spatiotemporal patterns from Eq. (1), and the middle column of **b, e, h, k, n**, and **q** the condensed structural eigenmodes, and the right column of **c, f, i, l, o**, and **r** shows the visualization of the structural eigenmodes of the middle column.

typical condensations where (a–c) and (d–f) represent the case of global brain network, (g–i) and (j–l) the case of right hemisphere, and (m–o) and (p–r) the case of the cognitive network of medial default mode. The left column of (a), (d), (g), (j), (m) and (p) represents the spatiotemporal patterns from Eq. (1), the middle column of (b), (e), (h), (k), (n) and (q) the condensed structural eigenmodes, and the right column of (c), (f), (i), (l), (o) and (r) the visualization of the structural eigenmodes of the middle column. We observe that all the spatiotemporal patterns are typical chimera states and that all the condensed structural eigenmodes  $V_j$  are limited to the smaller eigenmodes with  $j \leq 12$ , confirming again that the condensation is limited only to the lower structural eigenmodes.

**Case of isolated cognitive subnetworks.** As mentioned in the previous section, not all of the nodes in the global brain network are activated for a specific task. Rather, only those nodes within a concrete cognitive subnetwork are activated. Supporting evidence for this claim includes that populations of neurons in the mammalian cerebral cortex are continuously active during purposeful behavior, as well as during resting and sleep<sup>41</sup>. These cognitive networks are most commonly detected in the resting state, task-focused behavior, or across both behavioral states. In this sense, the inactive nodes do not take part in the activities of Eq. (1) and should be removed from the network matrix  $W$ . Here, we follow this concept to consider only the connections within a cognitive network while removing all those connections between this cognitive network and the other seven cognitive networks, i. e., creating a case of isolated cognitive networks. After this operation, we surprisingly find that for all the eight cognitive networks in Figs. S4 and S5 in Supplementary Note 1, only the three networks of the medial default mode, motor & somatosensory, and visual systems are well connected as a whole, while the other five networks are divided into several separated parts, indicating that they are not suitable candidates for eigenmode analysis (see Supplementary Note 1). Thus, we hereby only focus on the three networks of the medial default mode, motor & somatosensory,

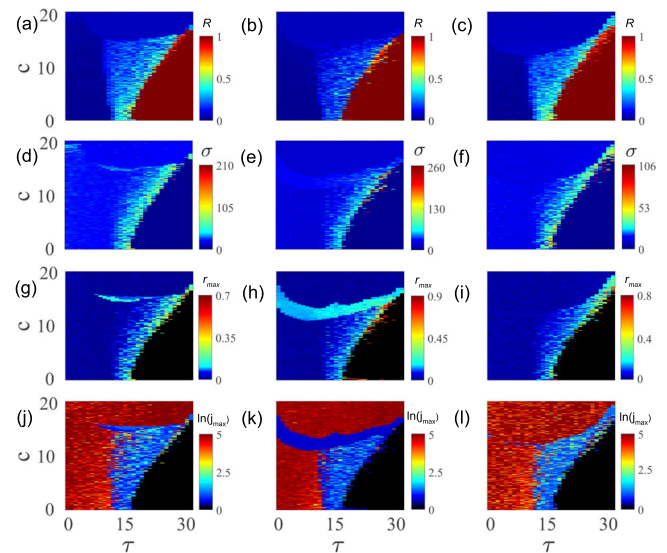


**Fig. 5 Phase diagrams for the case of isolated cognitive networks.** Phase diagrams on the parameter space  $\tau - c$  plane where the first to third columns represent the three networks: medial default mode, motor & somatosensory, and visual systems, respectively. These three cognitive networks are strongly connected and thus are suitable candidates for eigenmode analysis. **a-c** represent the phase diagrams of  $R$  on the parameter space  $\tau - c$  plane for the three cases, respectively. **d-f** represent the phase diagrams of  $\sigma(\tau, c)$  on the parameter space  $\tau - c$  plane, corresponding to **a-c**, respectively. **g-i** represent the phase diagrams of  $r_{max}$  corresponding to **a-c**, respectively. and **j-l** distributions of  $j_{max}$  corresponding to **a-c**, respectively.

and visual systems but discuss the other five cognitive networks in Supplementary Note 2B. In detail, we perform the same steps of Eqs. (1) and (2) to discuss the dependence of the order parameter  $R$  on the parameters  $\tau$  and  $c$ . Fig. 5a–c shows the phase diagrams of  $R$  on the parameter space  $\tau - c$  plane, where (a–c) represent the cases of the medial default mode, motor & somatosensory, and visual systems, respectively. Comparing Fig. 5a with its corresponding to Fig. 1k, we see that they are similar to each other, indicating that the feature of the chimera state remains unchanged.

Furthermore, we perform the same steps of Eq. (7) to discuss the dependence of the functional eigenmodes on the structural eigenmodes. We interestingly find that the condensation can still be observed. Fig. 5d–l shows the results of  $\sigma(\tau, c)$ ,  $r_{max}$  and  $j_{max}$  where the first, second, and third columns represent the cases of the medial default mode, motor & somatosensory, and visual systems, respectively, and the second, third, and fourth rows represent the values of  $\sigma(\tau, c)$ ,  $r_{max}$  and  $j_{max}$  respectively. Comparing the panels of Fig. 5 each other, we see that all of these panels have a specific narrow region where  $c$  is proportional to  $\tau$ . We also notice that these narrow regions of Fig. 5 are similar to that of the third column of Fig. 3. Therefore, the isolated networks can also show the features of condensation in the same parameter region as that embedded in the global brain network. Therefore, we conclude that condensation may be an intrinsic feature of brain functioning and a new window to understand the microscopic mechanism of brain functions.

Similar to Fig. 4, we hereby also show examples of typical condensations for the cases of isolated networks. Fig. 6 shows the results where (a–c) and (d–f) represent the case of the medial default mode with ( $c = 0.525, \tau = 15$ ) in (a–c) and ( $c = 0.725, \tau = 14$ ) in (d–f), (g–i) and (j–l) the case of the motor & somatosensory with ( $c = 0.025, \tau = 17$ ) in (g–i) and ( $c = 0.55,$

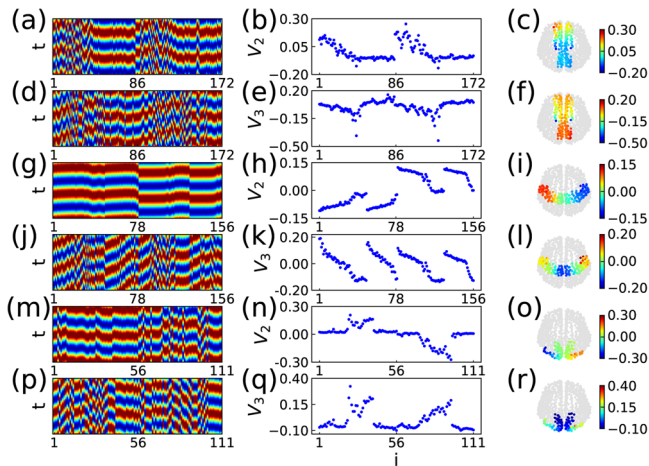


**Fig. 6 Condensations for the case of isolated cognitive networks.** Six typical condensations with the lower condensed eigenmodes for the three networks of Fig. 5 where **a-c** and **d-f** represent the case of the medial default mode with  $(c = 0.525, \tau = 15)$  in **a-c** and  $(c = 0.725, \tau = 14)$  in **d-f**, **g-i** and **j-l** the case of the motor & somatosensory with  $(c = 0.025, \tau = 17)$  in **g-i** and  $(c = 0.55, \tau = 16)$  in **j-l**, and **m-o** and **p-r** the case of the visual system with  $(c = 0.05, \tau = 15)$  in **(m)-(o)** and  $(c = 0.15, \tau = 13)$  in **p-r**. The left column of **a, d, g, j, m,** and **p** represents the spatiotemporal patterns from Eq. (1), and the middle column of **b, e, h, k, n** and **q** the condensed structural eigenmodes, and the right column of **c, f, i, l, o,** and **r** shows the visualization of the structural eigenmodes of the middle column.

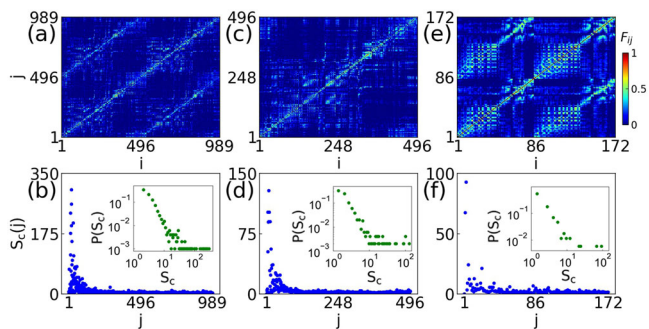


**Fig. 7 Evidence of condensation from the empirical data of resting-state functional connectivity (rsFC)**<sup>27</sup>. **a, b** represent the case of global brain network, **c, d** the case of right hemisphere, and **e, f** the case of medial default mode system. The first row represents the matrices  $\{F_{ij}\}$  of empirical rsFC of the three networks, and the second row represents their contributions  $S_c(j)$  of the  $j$ -th structural eigenmode, where the insets represent their distributions  $P(S_c)$ .

$\tau = 16$  in **(j-l)**, and **(m-o)** and **(p-r)** the case of the visual system with  $(c = 0.05, \tau = 15)$  in **(m-o)** and  $(c = 0.15, \tau = 13)$  in **(p-r)**. The left column of **(a), (d), (g), (j), (m)** and **(p)** represents the spatiotemporal patterns from Eq. (1), the middle column of **(b), (e), (h), (k), (n)** and **(q)** represents the condensed structural eigenmodes, and the right column of **(c), (f), (i), (l), (o)** and **(r)** shows the visualization of the structural eigenmodes of the middle column. We observe that all the spatiotemporal patterns are typical chimera states and that all the condensed structural eigenmodes  $V_j$  are limited to smaller eigenmodes such as  $j \leq 3$ , confirming that condensation is only focused on the smaller structural eigenmodes.

**Case of empirical brain network.** Finally, we provide some experimental evidence in support of our proposed condensation

mechanism. For this purpose, we consider the empirical data of resting-state functional connectivity (rsFC) from Ref. <sup>27</sup>, which corresponds to the structural network of Fig. 1b. Fig. 7a shows the matrix  $\{F_{ij}\}$  of the empirical rsFC. Correspondingly, Fig. 7c, e show the matrices of the right hemisphere and medial default mode from **(a)**, respectively. Then, we follow Eq. (7) to calculate the contributions  $S_c(j)$  of the  $j$ -th structural eigenmode for the three networks of Fig. 7a, c, and e. Fig. 7b, d, and f show the results corresponding to **a, c,** and **e**, respectively, where the insets represent their distributions  $P(S_c)$ . We observe that all three distributions  $P(S_c)$  are power law, confirming this previously observed feature of the critical state<sup>3</sup>. We also notice that there are several largest  $S_c(j_{max})$  with smaller  $j_{max}$  in Fig. 7b, d, and f, confirming the previously observed condensation on a few lower structural eigenmodes.

**Conclusion**

Based on our results, we offer key takeaways:

- (i) Condensation and power law distributions have been revealed for both brain networks including globally coupled and isolated cognitive networks, indicating that the functions of these networks are intrinsic features of brain operation. As the region of condensation is the same as that of chimera states in the  $\tau - c$  plane, the condensation and chimera state may share a close relationship to the condensation process. In this sense, the condensation process may elucidate a possible mechanism for how a brain function is performed.
- (ii) We propose a nonlinear diffusion model of Eq. (1) with biologically relevant time delays, in contrast to the linear diffusion models without time delays in previous spectral graph analysis<sup>20-25</sup>. It is easy to notice from Fig. 8a, b that the edge weights  $W_{ij}$  are exponentially distributed and spanned several orders of magnitude. The authors of Refs. <sup>26,27</sup> reasoned that interregional physiological efficacies would not span such a large range and thus they resampled the fiber strengths into a Gaussian distribution. The resampling process was as follows: given  $E$  raw data values  $x_1, x_2, \dots, x_E$ , they generated  $E$  random samples  $r_1, r_2, \dots, r_E$  from a unit Gaussian distribution. Then, they replaced the smallest raw data value with the smallest randomly sampled value, the second-smallest raw data

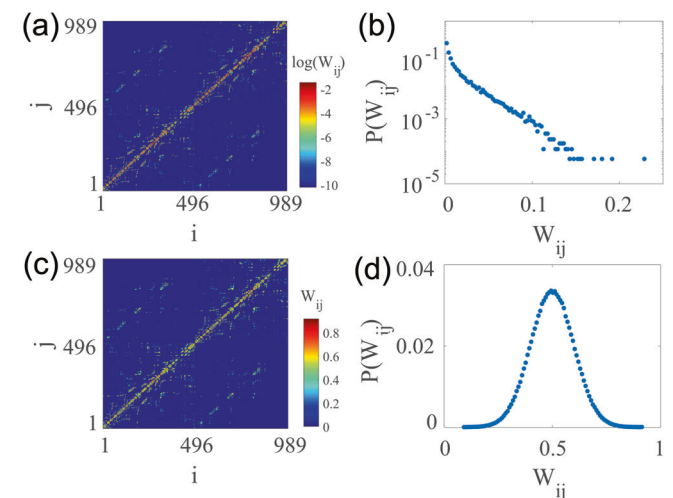


**Fig. 8 Edge weights  $W_{ij}$  of the structural brain network.** **a, b** represent the raw data, **c, d** represent the case of the resampled data. All these data are from Refs. <sup>26,27</sup>.

value with the second-smallest randomly sampled value, and so on until all raw data values are replaced. This set of  $E$  resampled data was then rescaled to a mean of 0.5 and a standard deviation of 0.1. More details are available in Refs. 26,27. Fig. 8c, d show the connectivity matrix  $W_{ij}$  and its distribution for the resampled data. It is easy to see from Fig. 8d that  $W_{ij}$  has a mean of 0.5. By carefully checking these data and letting each of the 998 ROIs be a node, we surprisingly find that there are 9 isolated nodes, which have no connections to other nodes. These 9 nodes are consistently isolated in both the raw and resampled data. Considering the connection feature of the network, we remove these 9 isolated nodes, yielding a structural brain network of size  $N = 989$  nodes ( $N_r = 496$  and  $N_l = 493$  nodes in the right and left hemisphere, respectively). In total, there are 17865 links.

- (iii) Others have noted that chimera states are inextricably related to cognitive function of brain<sup>42,43</sup>, while we here show that the chimera states in Fig. 1 are closely related to the condensations in Fig. 3, indicating a potential relationship between condensation and brain functioning. Furthermore, we see from Fig. 3g–i that their condensed eigenmodes are approximately  $\ln(j_{max}) \approx 3.5, 3.0$  and  $2.5$ , respectively, indicating that the cognitive network has the smallest condensed eigenmodes. In this sense, we conclude that the condensation of the cognitive network is similar to the observations reported in<sup>21–23</sup>. Moreover, we observe from Fig. 3a–f that in the regions of condensation, the degree of condensation increases with the time delay  $\tau$  for a fixed  $c$  but decreases with increasing coupling  $c$  for a fixed  $\tau$ . Thus, the parameters  $c$  and  $\tau$  take the key role of temperature in BEC.

Except for these aspects, there are limitations of our findings in terms of the emergence of brain functions. For example, it is well known that different brain functions are performed by different cognitive networks, implying that different input signals can be distinguished by different local parts of brain structural network. However, our results do not study this aspect of brain function. In addition, specific brain function usually involves multimode signals and thus may depend on the cooperation of multiple cognitive networks, which remains an open question for further studies.

Thus far, all the results are based on the specific brain network of 989 nodes. In this sense, it is necessary to verify whether these results are robust across different parcellations. For this purpose, similar condensation scenarios have been found for a brain network of smaller scale, i.e., 76 nodes across nine cognitive systems (resting-state networks<sup>9</sup>). We provide further details in Supplementary Note 3. Therefore, our results are robust to the topologies of brain structural networks.

Finally, we notice that biologically, the time delay is not a constant but depends on the distance between two nodes in the brain network. To discuss the effect of distributed time delays, we have considered the case in Supplementary Note 4 that the time delay  $\tau_{ij}$  between nodes  $i$  and  $j$  is determined by  $\tau_{ij} = d_{ij}/v$ , where  $d_{ij}$  represents the distance between the nodes  $i$  and  $j$  and  $v$  is the conduction speed. We find that the distribution of time delays does have influence on the chimera states, but the close relationship between the condensation and chimera states still exists.

In conclusion, we used a structural network representation of the brain combined with a computational model of regional brain dynamics to study how structural eigenmodes are related to functional brain states. Specifically, we study the relationship between eigenmodes and chimera states. By considering a neural mass model of a population with a time delay, We show that chimera states can only be observed in an optimal region.

Surprisingly, we reveal a phenomenon of condensation in this optimal region where all the functional eigenmodes are condensed to a few or even a single structural eigenmode, but not in the nonoptimal region. The condensed eigenmodes are usually limited to the lower structural eigenmodes and the contributions of structural eigenmodes satisfy a power law distribution in the optimal region but demonstrate an exponential distribution in the nonoptimal region. Moreover, we show that condensation also appears in different levels of brain subnetworks, such as hemispheres and cognitive subnetworks, and even in isolated cognitive subnetworks and the empirical rsFC, indicating that condensation is a potential mechanism of broader brain function. Moreover, condensation may even be an intrinsic feature of brain functioning, which proposes a new framework for understanding the microscopic mechanism of brain functions.

## Methods

**A structural brain network with edge weights of Gaussian distribution.** For the network substrate, we employ the weighted network of the cerebral cortex from the data of Refs. 26,27, which was obtained by two steps. In the first step, 5 healthy right-handed male participants (age  $29.4 \pm 3.4$  years) were scanned on an Achieva 3T Philips scanner and a high-resolution. The T1-weighted gradient echo sequence was acquired in a matrix of  $512 \times 512 \times 128$  voxels of isotropic  $1 - mm$  resolution. Then, following diffusion spectrum and T1-weighted MRI acquisitions, the segmented gray matter was partitioned into 66 anatomical regions according to anatomical landmarks using FreeSurfer (surfer.nmr.mgh.harvard.edu) and 998 ROIs. White matter tractography was performed with a custom streamline algorithm, and finally, fiber connectivity was aggregated across all voxels within each of the 998 predefined ROIs. Further details are available in Refs. 26,27. Fig. 8a shows the connectivity matrix  $W_{ij}$  among the 998 ROIs, which is color coded by edge weights. Correspondingly, Fig. 8b shows the distribution of  $W_{ij}$ .

It is easy to notice from Fig. 8a, b that the edge weights  $W_{ij}$  are exponentially distributed and spanned several orders of magnitude. The authors of Refs. 26,27 reasoned that interregional physiological efficacies would not span such a large range and thus they resampled the fiber strengths into a Gaussian distribution. The resampling process was as follows: given  $E$  raw data values  $x_1, x_2, \dots, x_E$ , they generated  $E$  random samples  $r_1, r_2, \dots, r_E$  from a unit Gaussian distribution. Then, they replaced the smallest raw data value with the smallest randomly sampled value, the second-smallest raw data value with the second-smallest randomly sampled value, and so on until all raw data values are replaced. This set of  $E$  resampled data was then rescaled to a mean of 0.5 and a standard deviation of 0.1. More details are available in Refs. 26,27. Fig. 8c, d show the connectivity matrix  $W_{ij}$  and its distribution for the resampled data. It is easy to see from Fig. 8d that  $W_{ij}$  has a mean of 0.5.

By carefully checking these data and letting each of the 998 ROIs be a node, we surprisingly find that there are 9 isolated nodes, which have no connections to other nodes. These 9 nodes are consistently isolated in both the raw and resampled data. Considering the connection feature of the network, we remove these 9 isolated nodes, yielding a structural brain network of size  $N = 989$  nodes ( $N_r = 496$  and  $N_l = 493$  nodes in the right and left hemisphere, respectively). In total, there are 17865 links.

**Measures of chimera state.** To characterize the dynamic patterns of Eq. (1), we introduce an order parameter  $R$  as follows:

$$Re^{i\phi} = \frac{1}{N_s} \sum_{s=1}^{N_s} e^{i\theta_s}, \quad (2)$$

where  $R$  characterizes the phase coherence,  $\phi$  is the average phase, and  $\theta_j$  is the phase of oscillator  $j$ , and  $N_s$  is the number of oscillators. The value of  $R$  will be zero for a disordered state and unity for synchronized state and in between for chimera states. The phase variable of a general nonlinear oscillator not necessarily having a well-defined rotational center can be obtained based on the general idea of the curvature<sup>44,45</sup>, namely,  $\theta_j = \arctan(\dot{v}_j^i/\dot{v}_j^e)$  in our system.

As  $R$  describes the phase coherence of the whole system but not the coexistence of synchronized and desynchronized parts, Kemeth et al. introduced a quantity  $g_0$  to describe the fraction of synchronization in the chimera state<sup>40</sup>. Their idea is based on the local curvature for the spatial coherence, represented by the second derivative in the case of one spatial dimension. In this case, of one dimension, the local curvature  $D$  can be calculated as

$$Df \equiv f(x + \Delta x, t) - 2f(x, t) + f(x - \Delta x, t), \quad (3)$$

where  $f$  represents the spatial data on a snapshot at time  $t$ . Let  $D_m$  be the maximal value of  $|Df|$ .  $D_m$  represents the curvature of the oscillator with its two neighbors being shifted 180° in phase<sup>40</sup>. Thus,  $|Df|$  will be distributed between 0 and  $D_m$ . We see from Eq. (3) that  $|Df|$  equals zero in the synchronous regime and finite values with pronounced fluctuations in the desynchronized regime.

Letting  $g$  be the normalized probability density of  $|Df|$ ,  $g(|Df| = 0)$  is the fraction of spatially synchronous regimes. Thus,  $g(|Df| = 0)$  is unity for a complete synchronized state and zero for a complete desynchronized state, and a value between zero and unity for a chimera state. As numerical simulations have fluctuations, it was suggested that those points with  $|Df| < 0.01D_m$  should be considered synchronized, and otherwise desynchronized<sup>40</sup>. That is, the fraction of coherent regions can be calculated by

$$g_0(t) = \int_0^\delta g(t, |Df|) d|Df|, \quad (4)$$

with  $\delta = 0.01D_m$ . Therefore, we have  $g_0 = 1$  for complete coherence,  $g_0 \approx 0$  for desynchronization, and  $0 < g_0 < 1$  for chimera states.

**Method of eigenmode analysis.** To determine the hidden feature in the third and fourth rows of Fig. 1, we turn to the framework of eigenmode analysis<sup>20–23</sup>. Its idea is as follows. For the weighted connection matrix  $W_{ij}$  in Eq. (1), we let  $L = D - W$  be the Laplacian matrix, where  $D$  is the diagonal weighted degree matrix<sup>23,24</sup>. Then, the Laplacian matrix can be decomposed as  $L = V\lambda V^T$ , where  $\lambda$  are the structural eigenvalues in ascending order and  $V$  are the eigenvectors. Specifically, the first eigenmode with  $\lambda_1 = 0$  and  $V_1 = \frac{1}{\sqrt{N}}(1, 1, \dots, 1)^T$  represents a homogeneous state in which all nodes are equally involved, i.e., synchronization. Similarly, we can perform eigenmode analysis for functional networks. For this purpose, we first calculate the network dynamics  $u_i(t)$  ( $i = 1, 2, \dots, N$ ) from Eq. (1) for each pair of parameters  $(\tau, c)$  in Fig. 1(c) and then calculate all the Pearson correlation coefficients between any two of these  $N$  time series to obtain the functional brain network  $F$ <sup>46</sup>. After that, the matrix  $F$  will be decomposed as  $F = U\Lambda U^T$ , where  $U$  represents the functional eigenvectors and  $\Lambda$  denotes the eigenvalues in ascending order<sup>24,25</sup>.

Considering that the structural eigenvectors  $V$  are mutually orthogonal with  $V_i^T V_i = 1$  and  $V_i^T V_j = 0$ , we may use them as a set of orthogonal bases to represent a  $N$  dimensional variable, such as  $U$ . In this way, we have

$$U_i = \sum_{j=1}^N m_{ij} V_j, \quad (i = 1, 2, \dots, N) \quad (5)$$

where  $(m_{ij})$  is the transformation matrix with  $\sum_{j=1}^N (m_{ij})^2 = 1$  and can be calculated by  $m_{ij} = V_j^T U_i$ . Thus,  $m_{ij}$  represents the

coefficient of projecting the functional eigenvector  $U_i$  onto the structural eigen eigenvector  $V_j$ . Meanwhile, left-multiplying  $U_i^T$  to Eq. (5), we have

$$1 = \sum_{j=1}^N m_{ij} U_i^T V_j = \sum_{j=1}^N m_{ij} (V_j^T U_i)^T = \sum_{j=1}^N (m_{ij})^2, \quad (6)$$

indicating that  $m_{ij}$  satisfies the normalization condition.

Based on the projection coefficient  $m_{ij}$ , the contribution of the  $j$ -th structural eigenmode to the network dynamics through the  $i$ -th functional mode can be represented by  $(\Lambda_i m_{ij})^2$ <sup>24,25</sup>. Thus, the contribution of the  $j$ -th structural eigenmode to the functional network can be measured by its contribution over all the functional modes

$$S_c(j) = \sum_{i=1}^N (\Lambda_i m_{ij})^2. \quad (7)$$

For a dynamic pattern with a set of specific parameters  $(\tau, c)$ , the values of  $S_c(j)$  will be different for different  $j$ , i.e., a distributed  $S_c(j)$ . For different sets of parameters  $(\tau, c)$ , the eigenvalues  $\Lambda_i$  will be different, and thus, their distributions of  $S_c(j)$  will also be different.

#### Data availability

Data generated during the study is available upon request from the authors (E-mail: zhliu@phy.ecnu.edu.cn).

#### Code availability

The code used during the study is available upon request from the authors (E-mail: zhliu@phy.ecnu.edu.cn).

Received: 19 October 2022; Accepted: 26 September 2023;

Published online: 07 October 2023

#### References

- Bianconi, G. & Barabasi, A. Bose-Einstein condensation in complex networks. *Phys. Rev. Lett.* **86**, 5632 (2001).
- Sun, Y. et al. Eigen microstates and their evolutions in complex systems. *Commun. Theor. Phys.* **73**, 065603 (2021).
- Toker, D. et al. Consciousness is supported by near-critical cortical electrodynamics. *Proc. Natl Acad. Sci. USA* **119**, e2024455119 (2022).
- Harlow, J. M. Passage of an iron rod through the head. *Boston Med. Surg. J.* **39**, 389 (1848).
- Scoville, W. B. & Milner, B. Loss of recent memory after bilateral hippocampal lesions. *J. Neurol. Psychiatry* **20**, 11 (1957).
- Bullmore, E. & Sporns, O. Complex brain networks: graph theoretical analysis of structural and functional systems. *Nat. Rev. Neurosci.* **10**, 186 (2009).
- Fornito, A., Zalesky, A. & Breakspear, M. The connectomics of brain disorders. *Nat. Rev. Neurosci.* **16**, 159 (2015).
- Huo, S. et al. Spatial multi-scaled chimera states of cerebral cortex network and its inherent structure-dynamics relationship in human brain. *Natl Sci. Rev.* **8**, nwaal25 (2021).
- Bansal, K. et al. Cognitive chimera states in human brain networks. *Sci. Adv.* **5**, eaau8535 (2019).
- Huo, S., Zou, Y., Kaiser, M. & Liu, Z. Time-limited self-sustaining rhythms and state transitions in brain networks. *Phys. Rev. Res.* **4**, 023076 (2022).
- Buzsaki, G. *Rhythms of the Brain*. (Oxford University Press, New York, 2006).
- Majhi, S., Bera, B. K., Ghosh, D. & Perc, M. Chimera states in neuronal networks: a review. *Phys. Life Rev.* **28**, 100 (2019).
- Wang, Z. & Liu, Z. A brief review of chimera state in empirical brain networks. *Front. Physiol.* **11**, 724 (2020).
- Wu, T., Zhang, X. & Liu, Z. Understanding the mechanisms of brain functions from the angle of synchronization and complex network. *Front. Phys.* **17**, 31504 (2022).
- Abrams, D. M. & Strogatz, S. H. Chimera states for coupled oscillators. *Phys. Rev. Lett.* **93**, 174102 (2004).
- Parastesh, F. et al. Chimeras. *Phys. Rep.* **898**, 1 (2021).

17. Wang, Z. et al. Chimeras in an adaptive neuronal network with burst-timing-dependent plasticity. *Neurocomputing* **406**, 117 (2020).
18. Hussain, I., Jafari, S., Perc, M. & Ghosh, D. Chimera states in a multi-weighted neuronal network. *Phys. Lett. A* **424**, 127847 (2022).
19. Tamaki, M. et al. Night watch in one brain hemisphere during sleep associated with the first-night effect in humans. *Curr. Biol.* **26**, 1190 (2016).
20. Wang, M. B., Owen, J. P., Mukherjee, P. & Raj, A. Brain network eigenmodes provide a robust and compact representation of the structural connectome in health and disease. *PLoS Comput. Biol.* **13**, e1005550 (2017).
21. Abdelnour, F., Dayan, M., Devinsky, O., Thesen, T. & Raj, A. Functional brain connectivity is predictable from anatomic network's Laplacian eigen-structure. *NeuroImage* **172**, 728 (2018).
22. Raj, A., Kuceyeski, A. & Weiner, M. A network diffusion model of disease progression in dementia. *Neuron* **73**, 1204 (2012).
23. Atasoy, S., Donnelly, I. & Pearson, J. Human brain networks function in connectome-specific harmonic waves. *Nat. Commun.* **7**, 10340 (2016).
24. Wang, R. et al. Hierarchical connectome modes and critical state jointly maximize human brain functional diversity. *Phys. Rev. Lett.* **123**, 038301 (2019).
25. Wang, R. et al. Segregation, integration, and balance of large-scale resting brain networks configure different cognitive abilities. *Proc. Natl Acad. Sci. USA* **118**, e2022288118 (2021).
26. Hagmann, P. et al. Mapping the structural core of human cerebral cortex. *PLoS Biol.* **6**, e159 (2008).
27. Honey, C. J. et al. Predicting human resting-state functional connectivity from structural connectivity. *Proc. Natl Acad. Sci. USA* **106**, 2035 (2009).
28. Wendling, F., Bellanger, J. J., Bartolomei, F. & Chauvel, P. Relevance of nonlinear lumped-parameter models in the analysis of depth-EEG epileptic signals. *Biol. Cybern.* **83**, 367 (2000).
29. Zhou, C., Zemanova, L., Zamora-Lopez, G., Hilgetag, C. C. & Kurths, J. Structure Cfunction relationship in complex brain networks expressed by hierarchical synchronization. *N. J. Phys.* **9**, 178 (2007).
30. David, O., Harrison, L. & Friston, K. J. Modelling event-related responses in the brain. *NeuroImage* **25**, 756 (2005).
31. Huntenburg, J. M., Bazin, P.-L. & Margulies, D. S. Large-scale gradients in human cortical organization. *Trends Cogn. Neurosci.* **22**, 21 (2018).
32. Vicente, R., Gollo, L. L., Mirasso, C. R., Fischer, I. & Pipa, G. Dynamical relaying can yield zero time lag neuronal synchrony despite long conduction delays. *Proc. Natl Acad. Sci. USA* **105**, 17157 (2008).
33. Izhikevich, E. M. Polychronization: computation with spikes. *Neural Comput.* **18**, 245 (2006).
34. Adhikari, B. M., Prasad, A. & Dhamala, M. Time-delay-induced phase-transition to synchrony in coupled bursting neurons. *Chaos* **21**, 023116 (2011).
35. Dhamala, M., Jirsa, V. K. & Ding, M. Enhancement of neural synchrony by time delay. *Phys. Rev. Lett.* **92**, 074104 (2004).
36. Swadlow, H. A. Monitoring the excitability of neocortical efferent neurons to direct activation by extracellular current pulses. *J. Neurophysiol.* **68**, 605 (1992).
37. Swadlow, H. A. Efferent neurons and suspected interneurons in motor cortex of the awake rabbit: axonal properties, sensory receptive fields, and subthreshold synaptic inputs. *J. Neurophysiol.* **71**, 437 (1994).
38. Milton, J., and Jung, P., *Epilepsy as a dynamic disease* (Berlin: Springer, 2003).
39. Kandel, E. R., Schwartz, J. H., and Jessell, T.M., *Principles of Neural Science* (Elsevier, New York, 1991), 3rd ed.
40. Kemeth, F. P., Haugland, S. W., Schmidt, L., Kevrekidis, I. G. & Krischer, K. A classification scheme for chimera states. *Chaos* **26**, 094815 (2016).
41. Gusnard, D. A. & Raichle, M. E. Searching for a baseline: functional imaging and the resting human brain. *Nat. Rev. Neurosci.* **2**, 685 (2001).
42. Hagerstrom, A. M. et al. Experimental observation of chimeras in coupled-map lattices. *Nat. Phys.* **8**, 658 (2012).
43. Martens, E. A., Thutupalli, S., Fourriere, A. & Hallatschek, O. Chimera states in mechanical oscillator networks. *Proc. Natl Acad. Sci. USA* **110**, 10563 (2013).
44. Osipov, G. V., Hu, B., Zhou, C., Ivanchenko, M. V. & Kurths, J. Three types of transitions to phase synchronization in coupled chaotic oscillators. *Phys. Rev. Lett.* **91**, 024101 (2003).
45. Liu, Z., Zhou, J. & Munakata, T. Detecting generalized synchronization by the generalized angle. *Europhys. Lett.* **87**, 50002 (2009).
46. Eguiluz, V. M. et al. Scale-free brain functional networks. *Phys. Rev. Lett.* **94**, 018102 (2005).

## Acknowledgements

We thank C.S. Zhou for the critical comments. This work was partially supported by STI2030-Major Projects 2021ZD0202600 and the NNSF of China under Grant nos. 11835003, 82161148012, and 12175070 and the China Postdoctoral Science Foundation 2023M731114.

## Author contributions

Z.L. and S.H. conceived the experiment; S.H. developed the code and performed the numerical simulations; Z.L. and S.H. analyzed the results; Z.L. wrote the paper with contributions from all authors.

## Competing interests

The authors declare no competing interests.

## Additional information

**Supplementary information** The online version contains supplementary material available at <https://doi.org/10.1038/s42005-023-01405-8>.

**Correspondence** and requests for materials should be addressed to Zonghua Liu.

**Peer review information** *Communications Physics* thanks the anonymous reviewers for their contribution to the peer review of this work. A peer review file is available.

**Reprints and permission information** is available at <http://www.nature.com/reprints>

**Publisher's note** Springer Nature remains neutral with regard to jurisdictional claims in published maps and institutional affiliations.



**Open Access** This article is licensed under a Creative Commons Attribution 4.0 International License, which permits use, sharing, adaptation, distribution and reproduction in any medium or format, as long as you give appropriate credit to the original author(s) and the source, provide a link to the Creative Commons license, and indicate if changes were made. The images or other third party material in this article are included in the article's Creative Commons license, unless indicated otherwise in a credit line to the material. If material is not included in the article's Creative Commons license and your intended use is not permitted by statutory regulation or exceeds the permitted use, you will need to obtain permission directly from the copyright holder. To view a copy of this license, visit <http://creativecommons.org/licenses/by/4.0/>.

© The Author(s) 2023